Article

A Novel Non-Isolated Three-Port Bidirectional DC/DC Converter for Photovoltaic Electric Scooter Charging Stations

Yu-En Wu *[ID] **and Xiu-Yi Lin**

Department of Electronic Engineering, National Kaohsiung University of Science and Technology,
Kaohsiung 824, Taiwan; F107112106@nkust.edu.tw

* Correspondence: yew@nkust.edu.tw; Tel.: +886-7-6011000 (ext. 32511)

check for
updates

Abstract: This paper proposes a novel non-isolated three-port bidirectional dc/dc converter for photovoltaic (PV) electric scooter (ES) charging stations. The proposed converter combines an improved boost converter and a bidirectional buck-boost converter. When the PV energy is sufficient, the PV module is stepped up to provide dc load energy to the ES through the improved boost converter in order to charge the ES battery. When the PV energy is insufficient, the storage battery is stepped up to provide energy to the ES load dc bus, and the ES load dc bus charges the battery if the battery energy is low. The proposed converter reduces the number of components and circuit cost by using a switch internal diode. Finally, a 400-W modified boost converter and a 120-W/60-W bidirectional boost-buck converter were implemented to verify the three operating modes of the proposed non-isolated dc/dc converter. The results revealed that the highest efficiency levels achieved under PV module step-up, storage battery step-up, and storage battery step-down operation were 97.5%, 96.6%, and 92%, respectively.

Keywords: three-port bidirectional converter; photovoltaic (PV) electric scooter (ES) charging stations

1. Introduction

With the increasing awareness of environmental protection, solar power has come to be regarded as an attractive energy source. Solar panels have become optimal representatives of green energy under strong sunlight conditions. In addition, pollutants such as carbon dioxide, sulfur dioxide, nitrogen oxides, PM2.5, and volatile organic compounds are becoming considerably critical. People are paying attention to carbon dioxide and waste generated from gasoline and diesel vehicles. People are gradually accepting electric vehicles (EVs) because of their cleanness; moreover, EVs have become mainstream in several countries worldwide [1]. In Taiwan, because of the narrow roads and dense population, motorcycles constitute the primary transportation vehicles. Asia has the highest density of motorcycles in the world. In recent years, the popularity of electric scooters (ESs) has increased gradually. Although ES use can reduce fuel emissions, it is still marred by several limitations. For example, the power supply of ESs is a major problem for ES riders. Additional drawbacks include the limited availability of charging stations, large battery storage space, long charging time, and battery life.

Despite the aforementioned limitations, ESs have become a major factor in the future development of transportation systems in Taiwan; hence, improving ES charging systems is becoming increasingly crucial. Accordingly, photovoltaic (PV) power generation and ES charging have been combined to construct a highly convenient and environmentally friendly system. The market share of ESs is expected to grow substantially [2].

In general, a large gap exists between the output voltage of green energy systems and the voltage demand of an ES bus (load bus). Therefore, a set of boost converters is required. Only traditional boost,

single-ended step-up, converters are used for ESs. Converters cannot be combined with energy storage systems to develop a converter system [3]. To effectively charge and discharge energy storage systems, a bidirectional buck-boost circuit is required [4]. In addition, a bidirectional buck-boost circuit should be used to step-up green energy to the ES bus. These requirements cannot be realized using traditional converters [5–14]. Accordingly, this study developed a novel nonisolated three-port bidirectional dc/dc converter for PV ES charging stations.

Figure 1 illustrates a block diagram of a green energy application. Green energy such as PV or wind energy constitutes the energy source of the dc/dc converter, and the design objective of this converter is to achieve high efficiency, small size, and low cost. Energy storage systems for PV system applications currently constitute a major research direction for scholars. In a system with battery energy storage, the storage battery voltage may differ considerably from the load bus terminal voltage; hence, a dc/dc converter with a step-up function is also required. Moreover, a step-down converter is required to charge the storage battery. Therefore, bidirectional converters that can achieve step-up and step-down functions in the same topology should be designed. Accordingly, reducing the size, cost, and component count of converters is a critical problem. Recently, several non-isolated [15–17] and isolated [18–24] bidirectional converters have been proposed for conversion of different voltages.
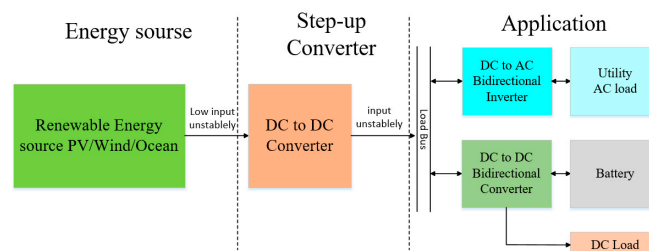

Figure 1. Block diagram of green energy application.

A previous study proposed an improved boost/buck bidirectional converter with step-up/step-down functions and a substantial cost; however, its boost and buck efficiencies are poor [25]. Furthermore, [26] is presented an improved boost/buck converter with a coupling inductor. The topology for this converter comprises two switches and a coupling inductor; its output power is only 100 W and efficiency is low. Another study developed a bidirectional converter between a battery terminal and dc bus terminal with a transformer [27]; the topology for this converter comprises four switches used to implement a 200-W output power. The staggered control method reduces the input ripple current but increases the complexity of its control and circuit.

Recently, several scholars have proposed three-terminal converter topologies [28–31]. Specifically, [28] proposed a non-isolated three-port converter with an energy storage system and PV. In this topology, a relatively high number of operating modes, switches, and diode components are used, resulting in poor efficiency. The converter proposed in [29] is based on an isolated topology with a transformer as well as three switches and four Schottky diodes; an LCL resonant circuit is also added to the primary side. However, the disadvantages of this topology are its complex structure, high cost, and poor efficiency. In [30], a unidirectional converter and bidirectional converter were combined with an energy storage system; this converter is based on a highly complicated and isolated topology comprising two switches and four Schottky diodes. However, the output power of the converter is only 150 W, and it cannot efficiently execute charge/discharge and power supply to the load bus simultaneously.

Figure 2 illustrates the proposed three-port bidirectional converter. When the PV energy is sufficient, the battery is charged and energy is supplied to the dc bus. When the PV energy is insufficient, the battery can supply energy to the dc bus. This topology contains different operating modes; thus, it can considerably reduce the circuit cost and size.
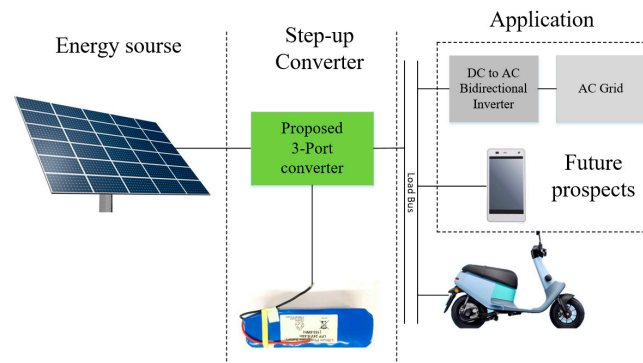
Figure 2. Three-port bidirectional converter application.

2. Proposed Converter and Operating Principles

Figure 3 illustrates the proposed three-port non-isolated step-up/step-down bidirectional dc/dc converter for PV ES charging stations. The converter topology comprises a unidirectional boost converter combined with an improved bidirectional buck/boost converter. The unidirectional boost converter is used to step up the PV module output to the ES load bus. The bidirectional buck/boost converter serves as the interface between the storage battery and ES load bus. If the energy of the ES load bus is sufficient, it is stepped down to charge the storage battery. However, if the energy of the ES load bus is insufficient, the storage battery output is stepped up to charge the ES load battery. The auxiliary inductance LBat at the port of the storage battery can change the output voltage of the ES load bus and provide a continuous current to charge the storage battery. The proposed topology focuses on combining PV energy, ES load battery, and storage battery energy; it comprises three switches (S_1–S_3), a Schottky diode (D_1), two inductors (L_{In} and L_{Bat}), and three capacitors (C_{In}, C_{Load}, and C_{Bat}).
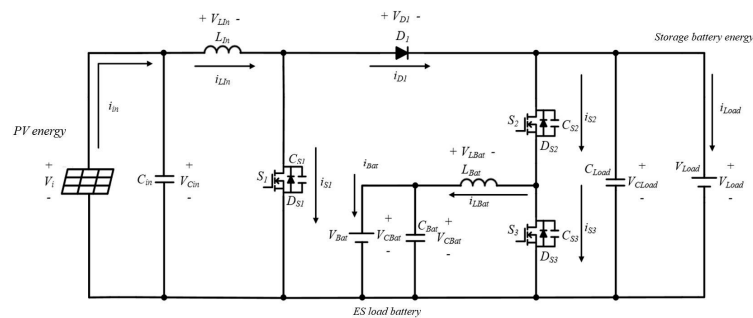

Figure 3. Proposed non-isolated three-port bidirectional dc/dc converter.

The proposed three-port bidirectional dc/dc converter involves three operating modes. In the first mode, when the PV energy is sufficient, the PV module output is stepped up to the ES bus to charge the ES battery. In the second mode, when the ES bus has sufficient energy, the output is stepped down to charge the storage battery. In the third mode, when the storage battery has sufficient energy and no PV output, the storage battery provides energy to the ES bus and charges the ES battery.

To simplify the circuit analysis, the following assumptions can be made:

(1) The capacitance levels of C_{in}, C_{Load}, and C_{Bat} are sufficiently high, and the output voltage can be maintained as a constant voltage source.
(2) All switches S_1, S_2, and S_3 and diode D_1 are ideal components.
(3) The inductor current is in continuous mode (maintains a positive value).
(4) The switching period is T, the turned-on time of the switches is DT, and the turned-off time of the switches is $1 - DT$.

A. Stage 1: The PV output voltage is stepped up to the ES bus to charge the ES battery

When the energy supplied from the PV modules is sufficient, the PV module voltage is stepped up to the ES bus to charge the ES battery. Figure 4 illustrates the waveform of the operation of the main components in Stage 1.
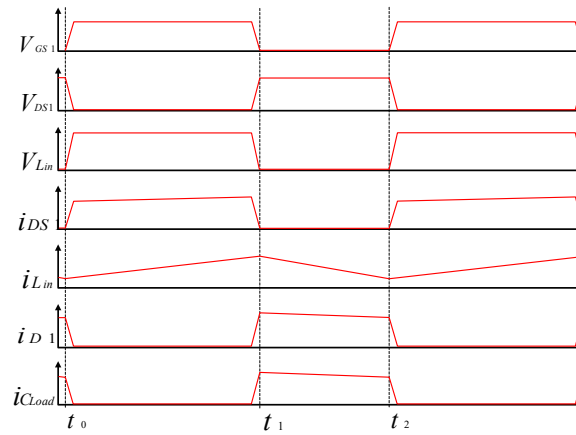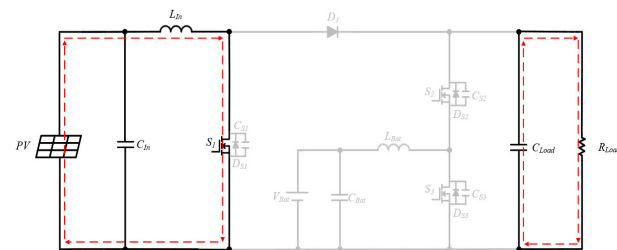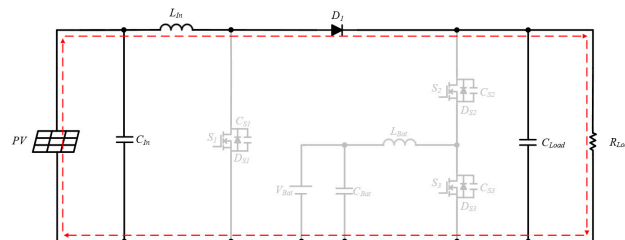
Figure 4. Waveforms obtained for the operation of the main components in Stage 1.

a. Mode 1 [$t_0 \leq t < t_1$]

When $t = t_0$, S_1 is turned on; S_2, S_3, and S_4 are turned off; and D_1 is turned off. Figure 5a presents the current flow direction. In this mode, the PV voltage provides energy for storage in the inductor L_{In}. At this time, the ES load is provided by C_{Load}.

(a) Mode 1

(b) Mode 2

Figure 5. Circuit operation in each mode in Stage 1: (a) Mode 1 and (b) Mode 2.

b. Mode 2 [$t_1 \leq t < t_2$]

When $t = t_1$, S_1 is turned off and S_2 and S_4 are continuously turned off. At this time, D_1 is turned on. Figure 5b presents the current flow direction. In this mode, the energy of the inductor L_{In} is supplied to the ES bus, and the ES battery is charged by D_1.

B.　Stage 2: ES bus is stepped down to charge storage battery

When the energy supplied by the PV modules is insufficient and the storage battery requires charging, the output voltage of the ES bus is stepped down to charge the storage battery. Figure 6 presents the waveforms of the operation of the main components in Stage 2.
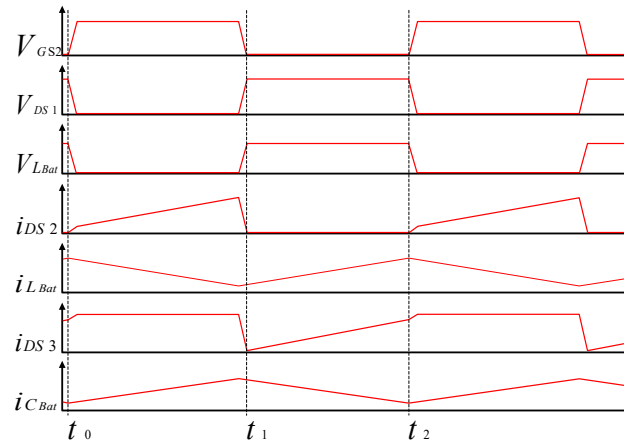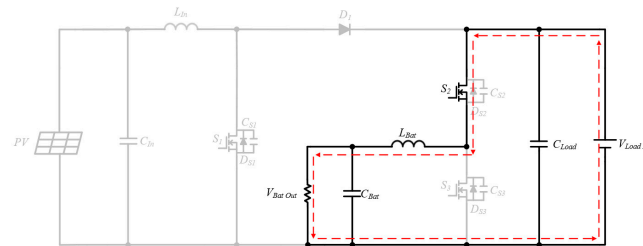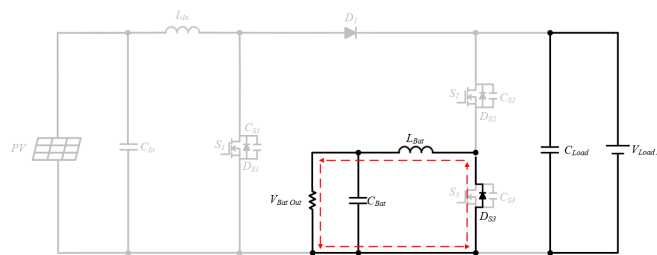

Figure 6. Waveforms obtained for the operation of main components in Stage 2.

a.　Mode 1 $[t_0 \leq t < t_1]$

When $t = t_0$, S_2 is turned on, S_1 and S_3 are turned off, and D_1 is turned off. Figure 7a presents the current flow direction. In this mode, the ES bus is used to store energy in the inductor L_{Bat}.

(**a**) Mode 1

(**b**) Mode 2

Figure 7. Circuit operation in each mode in Stage 2: Modes (**a**) 1 and (**b**) 2.

b.　Mode 2 $[t_1 \leq t < t_2]$

When $t = t_1$, S_1 and S_3 are continuously turned off and S_2 and D_1 are turned off. Figure 7b displays the current flow direction. In this mode, the body diode of the switch S_3 is turned on, and the capacitor C_{Bat} and inductor L_{Bat} release energy. The capacitor C_{Bat} and inductor L_{Bat} provide the energy at the output terminal of the energy storage battery.

C.   Stage 3: Storage battery provides energy to ES bus and charge the ES battery

When the energy supplied by the PV modules is insufficient, the storage battery is independently stepped up to the ES bus to charge the ES battery. Figure 8 presents the waveforms for the operation of the main components in Stage 3.
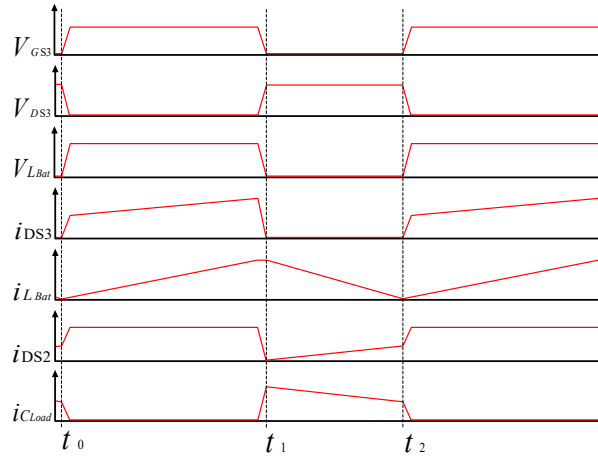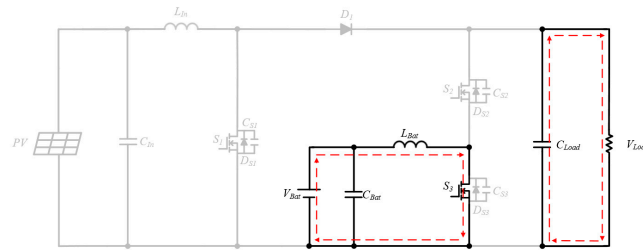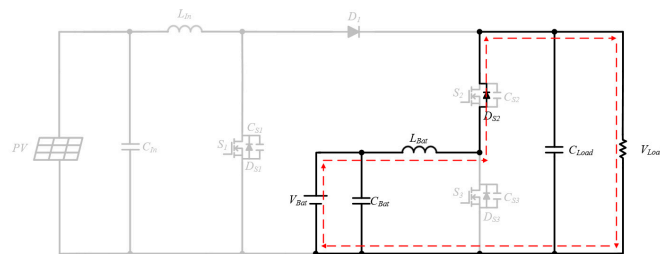

Figure 8. Waveforms obtained for the operation of the main components in Stage 3.

a.   Mode 1 $[t_0 \leq t < t_1]$

When $t = t_0$, S_3 is turned on, S_1 and S_2 are turned off, and D_1 is turned off. Figure 9a illustrates the current flow direction. In this mode, the storage battery is used to store energy in the inductor L_{Bat}. At this time, the energy of ES bus terminal is provided by C_{Load}.

(a) Mode I

(b) Mode 3

Figure 9. Circuit operation in each mode in Stage 3: Modes **(a)** 1 and **(b)** 2.

b.   Mode 2 $[t_1 \leq t < t_2]$

When $t = t_1$, S_3 is turned off, S_1 and S_2 are turned off, and the body diode of S_2 is turned on. Figure 9b displays the current flow direction. In this mode, the energy of the inductor L_{Bat} is provided to the ES bus, and the ES battery is charged by the body diode.

3. Operation Mode Conversion Analysis

In mode 1, when the main switch is turned off, the energy of L_{In} and PV is transferred to V_{Load} through the D_1 diode. When the energy of L_{In} is completely discharged and the circuit reaches the fully cut-off state, the power conversion of mode 2 can be performed.

In mode 2, when the main switch is turned off, the energy of L_{Bat} is transferred to V_{Bat} via the body diode of S_3. When the energy of L_{Bat} is completely discharged and the circuit reaches the fully cut-off state, the power conversion of mode 3 can be performed.

In mode 3, when the main switch is turned off, the energy of L_{Bat} and V_{Bat} is transferred to V_{Load} via the body diode of S_2. When the energy of L_{Bat} is completely discharged and the circuit reaches the fully cut-off state, it can go back to mode 2. Due to the simple circuit structure, the impact on transient energy conversion is small.

4. Steady-State Analysis

This section presents the mathematical derivation of the voltage conversion ratio and voltage stress of the components. First, the following assumptions can be made to simplify the analysis:

(1)   All components in the proposed topology are ideal components.
(2)   The capacitance is sufficiently large to maintain a constant voltage.
(3)   The system operates in a continuous conduction mode.

4.1. Voltage Conversion Ratio

Stage 1 is derived such that when PV energy is available, the PV module is stepped up to the ES bus to charge the ES battery. When the switch S_1 is turned on, the voltage on the magnetizing inductance L_{In} can be expressed as follows:

$$V_{L_{In}} = L_{In} \frac{di_{LIn}}{dt} = V_i \tag{1}$$

Because the rate of change of the inductor current is constant, when the switch is turned off, the current increases linearly with time. The change in the inductor current over time can be calculated as follows:

$$\frac{\Delta i_{L_{In}}}{\Delta t} = \frac{\Delta i_{L_{In}}}{DT} = \frac{V_i}{L_{In}} \tag{2}$$

Δi_{LIn} can be expressed as shown in Equation (3) when the switch is turned off:

$$\left(\Delta i_{L_{In}}\right)_{closed} = \frac{V_i DT}{L_{In}} \tag{3}$$

When S_1 is turned off (Figure 5), the inductor current does not change instantly, and the diode is turned on to provide the flow direction of the inductor current. If the output V_{CLoad} is constant, the voltage across the inductor can be expressed as follows:

$$V_{L_{In}} = \left(V_i - V_{C_{Load}}\right) = L_{In} \frac{di_{L_{In}}}{dt} \tag{4}$$

$$\frac{\left(V_i - V_{C_{Load}}\right)}{L_{In}} = \frac{di_{L_{In}}}{dt} \tag{5}$$

The rate of change of the inductor current is constant. The current changes linearly with time when the switch is turned off, and the change of the inductor current over time can be expressed as follows:

$$\frac{\Delta i_{L_{In}}}{\Delta t} = \frac{\Delta i_{L_{In}}}{(1-D)T} = \frac{\left(V_i - V_{C_{Load}}\right)}{L_{In}} \tag{6}$$

$$\left(\Delta i_{L_{In}}\right)_{open} = \frac{\left(V_i - V_{C_{Load}}\right)(1-D)T}{L_{In}} \tag{7}$$

According to the principle of voltage–second balance, the change of the inductor current must be zero under steady-state operation:

$$\left(\Delta i_{L_{In}}\right)_{closed} + \left(\Delta i_{L_{In}}\right)_{open} = 0 \tag{8}$$

$$\frac{V_i D T}{L_{In}} + \frac{\left(V_i - V_{C_{Load}}\right)(1-D)T}{L_{In}} = 0 \tag{9}$$

V_{CLoad} is expressed as follows:

$$V_i(D + 1 - D) - V_{C_{Load}}(1-D) = 0 \tag{10}$$

$$V_{C_{Load}} = \frac{V_i}{1-D} \tag{11}$$

$$GVo = \frac{V_{C_{Load}}}{V_i} = \frac{1}{1-D} \tag{12}$$

Mode 2 is derived when the energy at the ES load bus is sufficient. The voltage of the ES load bus is stepped down to charge the battery. When the switch is turned off (Figure 7), the diode is reverse biased, and the voltage across the inductor can be expressed as follows:

$$V_{L_{bat}} = V_{C_{Load}} - V_{Bat} = L_{Bat}\frac{di_{L_{Bat}}}{dt} \tag{13}$$

$$\frac{\Delta i_{L_{Bat}}}{\Delta t} = \frac{\left(V_{C_{Load}} - V_{Bat}\right)}{L_{Bat}} \tag{14}$$

Because the differential value of the current is a positive constant, the current increases linearly with time:

$$\frac{\Delta i_{L_{Bat}}}{\Delta t} = \frac{\Delta i_{L_{Bat}}}{DT} = \frac{\left(V_{C_{Load}} - V_{Bat}\right)}{L_{Bat}} \tag{15}$$

$$\left(\Delta i_{L_{Bat}}\right)_{closed} = \left(\frac{V_{C_{Load}} - V_{Bat}}{L_{Bat}}\right)DT \tag{16}$$

When the switch S_2 is turned off (Figure 7), the diode is forward biased to provide the flow direction of the inductor current. The voltage across the inductor is presented as follows:

$$V_{L_{bat}} = -V_{C_{Load}} = L_{Bat}\frac{di_{L_{Bat}}}{dt} \tag{17}$$

$$\frac{di_{L_{Bat}}}{dt} = \frac{-V_{Bat}}{L_{Bat}} \tag{18}$$

Because the differential value of the current is a negative constant, the current decreases linearly with time:

$$\frac{\Delta i_{L_{Bat}}}{\Delta t} = \frac{\Delta i_{L_{Bat}}}{(1-D)T} = \frac{-V_{Bat}}{L_{Bat}} \tag{19}$$

$$\left(\Delta i_{L_{Bat}}\right)_{open} = -\left(\frac{V_{Bat}}{L_{Bat}}\right)(1-D)T \tag{20}$$

According to the principle of voltage–second balance, the change of the inductor current within a cycle must be zero under steady-state operation:

$$\left(\Delta i_{L_{Bat}}\right)_{closed} + \left(\Delta i_{L_{Bat}}\right)_{open} = 0 \tag{21}$$

$$\left(\frac{V_{C_{Load}} - V_{Bat}}{L_{Bat}}\right)DT - \left(\frac{V_{Bat}}{L_{Bat}}\right)(1 - D)T = 0 \tag{22}$$

V_{Bat} is:

$$V_{Bat} = V_{C_{Loat}}D \tag{23}$$

$$GVo = \frac{V_{Bat}}{V_{C_{Load}}} = D \tag{24}$$

Mode 3 is derived when the energy storage battery has sufficient power but no PV energy. The energy storage battery provides energy to the ES load bus and charges the ES battery. When the switch is turned off (Figure 9), the diode is reverse biased. According to Kirchhoff's voltage law, V_{LBat} can be presented as follows:

$$V_{L_{Bat}} = L_{Bat}\frac{di_{L_{Bat}}}{dt} = V_{Bat} \tag{25}$$

Because the rate of change of the inductor current is constant, the current increases linearly with time. The change of the inductor current over time can be calculated as follows:

$$\frac{\Delta i_{L_{Bat}}}{\Delta t} = \frac{\Delta i_{L_{Bat}}}{DT} = \frac{V_{Bat}}{L_{Bat}} \tag{26}$$

Δi_{LBat} is presented in Equation (27) when the switch is turned off:

$$\left(\Delta i_{L_{Bat}}\right)_{closed=} \frac{V_{Bat}DT}{L_{Bat}} \tag{27}$$

When S_1 is turned off (Figure 9), the inductor current does not change instantaneously; therefore, the diode is forward biased to provide the flow direction of the inductor current. Assuming that the output V_{CLoad} is a fixed constant, the voltage across the inductor can be expressed as follows:

$$V_{L_{Bat}} = \left(V_{Bat} - V_{C_{Load}}\right) = L_{Bat}\frac{di_{L_{Bat}}}{dt} \tag{28}$$

$$\frac{\left(V_{Bat} - V_{C_{Load}}\right)}{L_{Bat}} = \frac{di_{L_{Bat}}}{dt} \tag{29}$$

The rate of change of the inductor current is constant; therefore, the current changes linearly with time. When the switch is turned off, the change of the inductor current over time can be expressed as follows:

$$\frac{\Delta i_{L_{Bat}}}{\Delta t} = \frac{\Delta i_{L_{Bat}}}{(1 - D)T} = \frac{\left(V_i - V_{C_{Load}}\right)}{L_{Bat}} \tag{30}$$

$$\left(\Delta i_{L_{Bat}}\right)_{open} = \frac{\left(V_{Bat} - V_{C_{Load}}\right)(1 - D)T}{L_{Bat}} \tag{31}$$

According to the principle of voltage–second balance, the change of the inductor current must be zero under steady-state operation:

$$\left(\Delta i_{L_{Bat}}\right)_{closed} + \left(\Delta i_{L_{Bat}}\right)_{open} = 0 \tag{32}$$

$$\frac{V_{Bat}DT}{L_{Bat}} + \frac{\left(V_{Bat} - V_{C_{Load}}\right)(1-D)T}{L_{Bat}} = 0 \tag{33}$$

V_{CLoad} is:

$$V_{Bat}(D + 1 - D) - V_{C_{Load}}(1 - D) = 0 \tag{34}$$

$$V_{C_{Load}} = \frac{V_{Bat}}{1 - D} \tag{35}$$

$$GVo = \frac{V_{C_{Load}}}{V_{Bat}} = \frac{1}{1 - D} \tag{36}$$

4.2. Voltage Stress of Components

The voltage stress of each component can be derived by analyzing the components' operation in the ON and OFF states.

The voltage stress of S_1 in the ON state in Mode 1 can be determined as presented in Figure 5a, and the corresponding switching stress can be expressed as follows:

$$V_i - V_{L_{In}} = 0 \tag{37}$$

Therefore, the voltage stress of S_1 can be derived as follows:

$$V_{S1} = \frac{1}{1 - D} V_i \tag{38}$$

The voltage stress of S_2 in the OFF state in Mode 2 can be determined as illustrated in Figure 7b, and the corresponding switching stress can be presented as follows:

$$V_{S2} = V_{Load} \tag{39}$$

The voltage stress of S_3 in the ON state in Mode 3 can be determined as displayed in Figure 9a, and the corresponding switching stress can be expressed as follows:

$$V_{Bat} - V_{L_{Bat}} = 0 \tag{40}$$

Therefore, the voltage stress of S_3 can be derived as follows:

$$V_{S3} = \frac{1}{1 - D} V_{Bat} \tag{41}$$

The voltage stress of the diode D_1 in the ON state in Mode 1 can be determined as shown in Figure 5a. The corresponding diode stress is the voltage across the ES load bus.

$$V_{D1} = V_{Load} \tag{42}$$

The voltage stress of input capacitor C_{In} is V_{In}:

$$V_{C_{In}} = V_{In} \tag{43}$$

The voltage stress of the output capacitor C_{Load} is V_{Load}:

$$V_{C_{Load}} = V_{Load} \tag{44}$$

The voltage stress of the output capacitor C_{Bat} is V_{Bat}:

$$V_{C_{Bat}} = V_{Bat} \tag{45}$$

5. Experimental Results and Analysis

Table 1 presents the electrical specifications and component parameters of the proposed nonisolated three-port bidirectional dc/dc converter.

Table 1. Electrical Specifications and Component Parameters of the Proposed Converter.

Parameter	Specification
Input PV voltage V_{in}	24 V
Battery voltage V_{Bat}	24 V
Load bus voltage V_{Load}	48 V
Maximus output battery power	60 W
Maximus output load bus power	400 W
Switching frequency fs	50 kHz

Component	Model	Specification
S_1, S_2, S_3	IRFP4332	250 V/57 A
D_1	MBR40200	200 V/40 A
C_{In}	Electrolytic Capacitor	100 µF/100 V
C_{Load}, C_{Bat}	Electrolytic Capacitor	470 µF/450 V
L_{In}, L_{Bat}	MPP Ring Core	100 µH

Figures 10–12 illustrate the efficiency curves obtained for the three operating modes of the proposed converter. As presented in Figure 10, in Mode 1, the efficiency was observed to be 97.45% under light-load operation (100 W), 95.8% under half-load operation (200 W), and 92.4% under full-load operation (400 W). The highest efficiency attained was 97.5% when the output power was 50 W. As displayed in Figure 11, in Mode 2, the highest efficiency was 92% under full-load operation (60 W), and the efficiency was observed to be 89.7% under half-load operation (30 W). Furthermore, in Mode 3, the efficiency levels were determined to be 97.7%, 97.4%, and 96.6% under light-load (29 W), half-load (60 W), and full-load (120 W) operation, respectively (Figure 12).
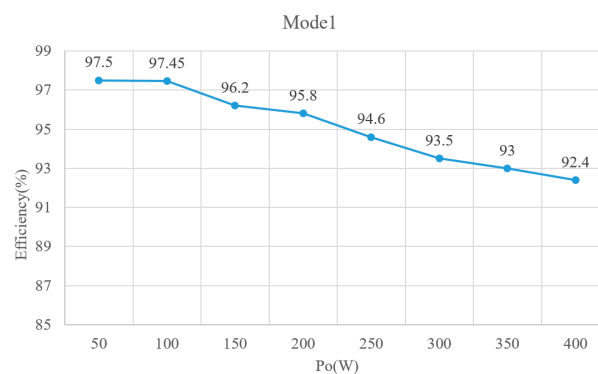

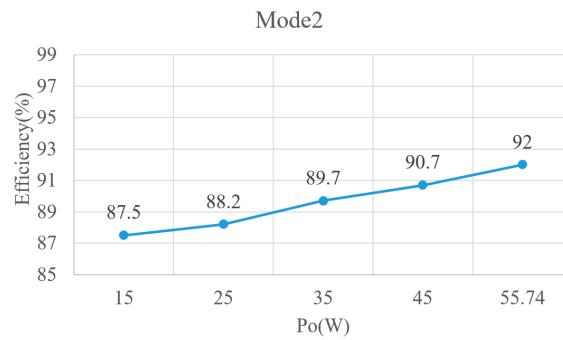**Figure 10.** Efficiency curves for the proposed converter in Mode 1 operation.

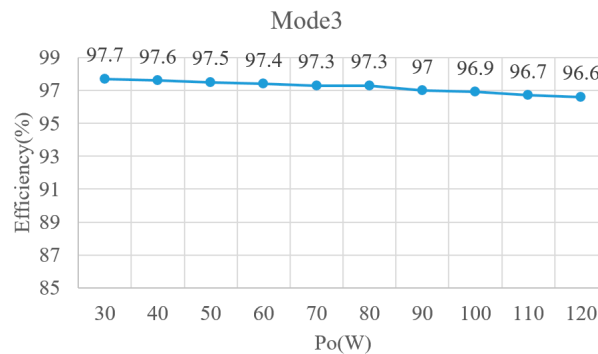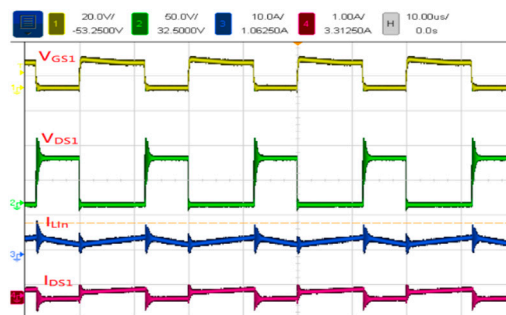**Figure 11.** Efficiency curves for the proposed converter in Mode 2 operation.

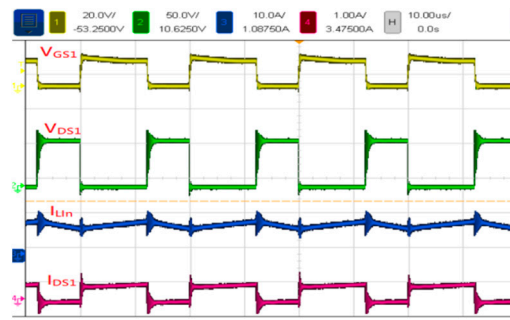**Figure 12.** Efficiency curves for the proposed converter in Mode 3 operation.

Figure 13 presents the voltage and current waveforms measured in Mode 1 at 100 W (light load) for S_1 and I_{DS1}. The duty cycle, input voltage, output voltage, input current, and output current of S_1 were 55.3%, 24 V, 58 V, 4.3 A, and 1.72 A, respectively. Additionally, the voltage stress of S_1 was 90 V, and the input current of L_{In} was 4.3 A.

(V_{GS1} (ch1): 20 V/div; V_{DS1} (ch2): 50 V/div; I_{LIn} (ch3): 10 A/div; and I_{DS1} (ch4): 1 A/div)

Figure 13. Voltage and current waveforms measured in Mode 1 at 100 W (light load).

Figure 14 presents the voltage and current waveforms measured in Mode 1 at 200 W (half load). The duty cycle, input voltage, output voltage, input current, and output current of S_1 were 55.8%, 24 V, 58 V, 8.7 A, and 3.44 A, respectively. The voltage stress of S_1 was 90 V, and the input current of L_{In} was 8.7 A (Figure 14a). Figure 14b shows the voltage and current waveforms of battery and output load operated under half load.

(V$_{GS1}$ (ch1): 20 V/div; V$_{DS1}$ (ch2): 50 V/div; I$_{LIn}$ (ch3): 10 A/div; and I$_{DS1}$ (ch4): 1 A/div)
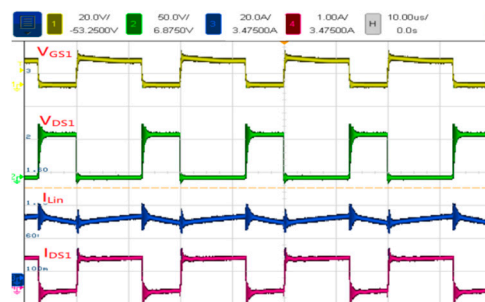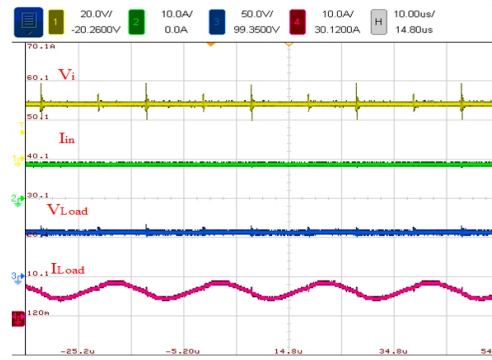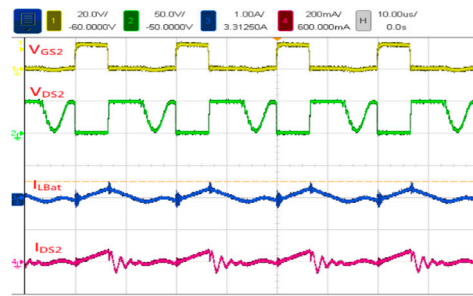
(**a**)

(V$_i$ (ch1): 20 V/div; I$_{in}$ (ch2): 10 A/div; V$_{Load}$ (ch3): 50 V/div; and I$_{Load}$ (ch4): 10 A/div)

(**b**)

Figure 14. Voltage and current waveforms measured in Mode 1 at 200 W (half load).

Figure 15 shows the voltage and current waveforms measured in Mode 1 at 400 W (full load). The duty cycle, input voltage, output voltage, input current, and output current of S_1 were 57.8%, 24 V, 58 V, 18.4 A, and 6.9 A, respectively. The voltage stress of S_1 was 90 V, and the input current of L_{In} was 18.4 A (Figure 15a). Figure 15b shows the voltage and current waveforms of battery and output load operated under full load.

(V$_{GS1}$ (ch1): 20 V/div; V$_{DS1}$ (ch2): 50 V/div; I$_{LIn}$ (ch3): 20 A/div; and I$_{DS1}$ (ch4) 1 A/div)

(**a**)

Figure 15. *Cont.*

(V$_i$ (ch1): 20 V/div; I$_{in}$ (ch2): 10 A/div; V$_{Load}$ (ch3): 50 V/div; and I$_{Load}$ (ch4): 10 A/div)

(**b**)

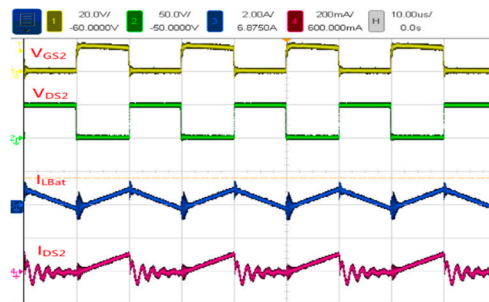**Figure 15.** Voltage and current waveforms measured in Mode 1 at 400 W (full load).

Figure 16 displays the voltage and current waveforms measured in Mode 2 at 14 W (light load) for I_{DS2} and S_2. The duty cycle, input voltage, output voltage, input current, and output current of S_2 were 41%, 58 V, 29.1 V, 0.3 A, and 0.5 A, respectively. The voltage stress of S_2 was 50 V, and the battery inductance L_{Bat} current was 0.5 A.

(V$_{GS2}$ (ch1): 20 V/div; V$_{DS2}$ (ch2): 50 V/div; I$_{LBat}$ (ch3): 1 A/div; and I$_{DS2}$ (ch4): 200 mA/div)

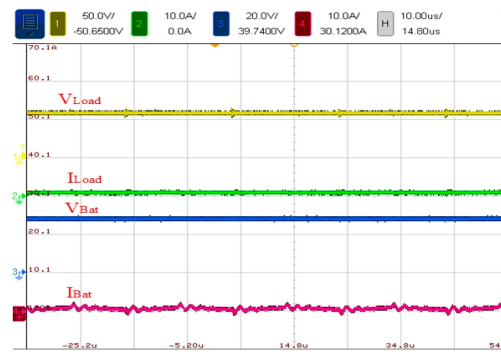**Figure 16.** Voltage and current waveforms of Mode 2 at 14 W (light load).

Figure 17 illustrates the voltage and current waveforms measured in Mode 2 at 30 W (half load). The duty cycle, input voltage, output voltage, input current, and output current of S_2 were 46. 6%, 58 V, 29 V, 0.53 A, and 0.95 A, respectively. The voltage stress of S_2 was 50 V, and the battery inductance L_{Bat} current was 0.95 A (Figure 17a). Figure 17b shows the voltage and current waveforms of battery and output load operated under half load.

(V$_{GS2}$ (ch1): 20 V/div; V$_{DS2}$ (ch2): 50 V/div; I$_{LBat}$ (ch3): 2 A/div; and I$_{DS2}$ (ch4): 200 mA/div)

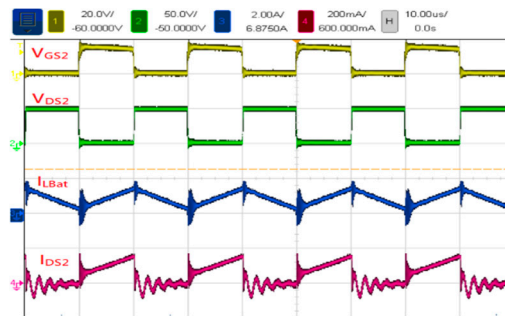(**a**)

Figure 17. *Cont.*

(V$_{Load}$ (ch1): 50 V/div; I$_{Load}$ (ch2): 10 A/div; V$_{Bat}$ (ch3): 20 V/div; and I$_{Bat}$ (ch4): 10 A/div)

(**b**)

Figure 17. Voltage and current waveforms measured in Mode 2 at 30 W (half load).

Figure 18 presents the voltage and current waveforms measured in Mode 2 at 60 W (full load). The duty cycle, input voltage, output voltage, input current, and output current of S_2 were 47.3%, 58 V, 29.1 V, 1.1 A, and 1.9 A, respectively. Moreover, the voltage stress of S_2 was 50 V, and the battery inductance L_{Bat} current was 1.9 A (Figure 18a). Figure 18b shows the voltage and current waveforms of battery and output load operated under full load.

(V$_{GS2}$ (ch1): 20 V/div; V$_{DS2}$ (ch2): 50 V/div; I$_{LBat}$ (ch3): 2 A/div; and I$_{DS2}$ (ch4): 200 mA/div)
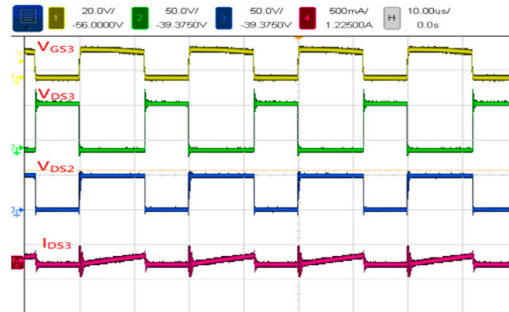
(**a**)

(V$_{Load}$ (ch1): 50 V/div; I$_{Load}$ (ch2): 10 A/div; V$_{Bat}$ (ch3): 20 V/div; and I$_{Bat}$ (ch4): 10 A/div)

(**b**)

Figure 18. Voltage and current waveforms measured in Mode 2 at 60 W (full load).
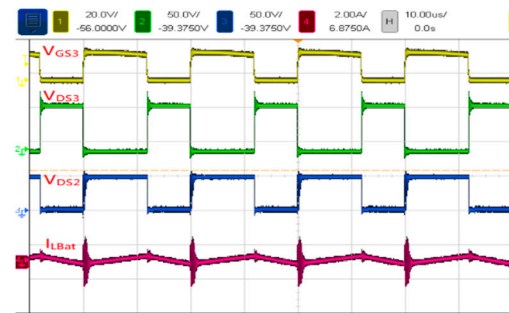
Figure 19 presents the voltage and current waveforms measured in Mode 3 at 30 W (light load). The duty cycle, input voltage, output voltage, input current, and output current of S_3 were 56.8%, 24 V, 59 V, 1.26 A, and 0.5 A, respectively (Figure 19a). The voltage stress of S_3 was 90 V, and the voltage

stress of S_2 was 50 V; the current waveform of I_{DS3} is also displayed in the figure. Figure 19b shows the voltage stress of S_3 to be 90 V and the voltage stress of S_2 to be 50 V; the current waveform of battery inductance L_{Bat} is also displayed in the figure.

(V_{GS3} (ch1): 20 V/div; V_{DS3} (ch2): 50 V/div; V_{DS2} (ch3): 50 V/div; and I_{DS3} (ch4): 500 mA/div)
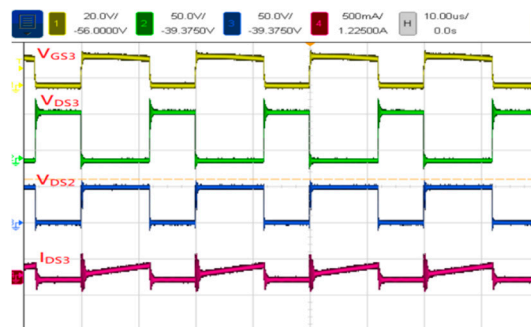
(**a**)

(V_{GS3} (ch1): 20 V/div; V_{DS3} (ch2): 50 V/div; V_{DS2} (ch3): 50 V/div; and I_{LBat} (ch4): 2 A/div)

(**b**)

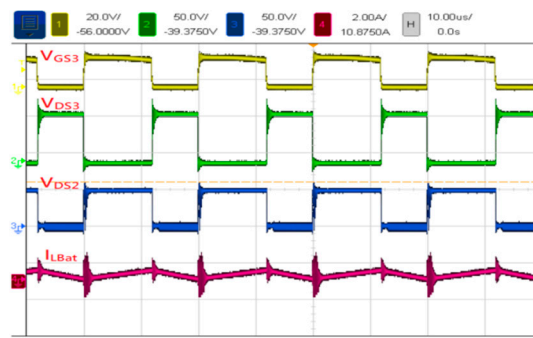**Figure 19.** Voltage and current waveforms measured in Mode 3 at 30 W (light load).

Figure 20 shows the voltage and current waveforms measured in Mode 3 at 60 W (half load). The duty cycle, input voltage, output voltage, input current, and output current of S_2 were 58%, 24 V, 59 V, 2.5 A, and 1 A, respectively (Figure 20a). The voltage stress levels of S_3 and S_2 were 90 and 50 V, respectively (Figure 20b). The control waveform of S_3 and current waveform of the battery inductance L_{Bat} are presented in the figures. Figure 20c shows the voltage and current waveforms of battery and output load operated under half load.

(V_{GS3} (ch1): 20 V/div; V_{DS3} (ch2): 50 V/div; V_{DS2} (ch3): 50 V/div; and I_{DS3} (ch4): 500 mA/div)
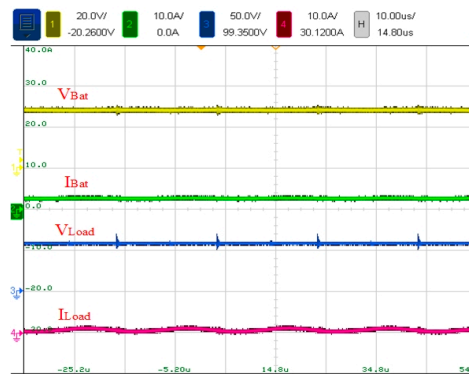
(**a**)

Figure 20. *Cont.*

(V$_{GS3}$ (ch1): 20 V/div; V$_{DS3}$ (ch2): 50 V/div; V$_{DS2}$ (ch3): 50 V/div; and I$_{LBat}$ (ch4): 2 A/div)
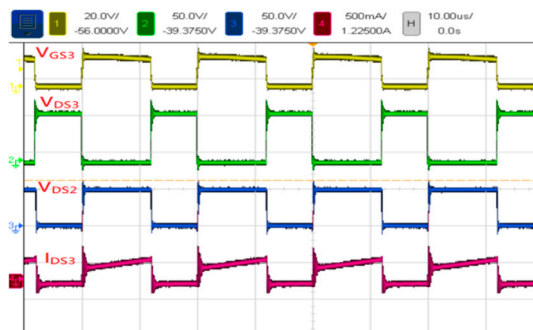
(**b**)

(V$_{Bat}$ (ch1): 20 V/div; I$_{Bat}$ (ch2): 10 A/div; V$_{Load}$ (ch3): 50 V/div; and I$_{Load}$ (ch4): 10 A/div)

(**c**)

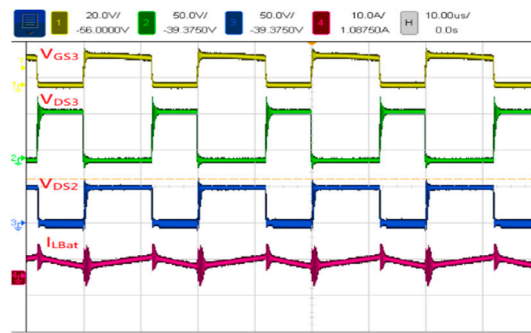**Figure 20.** Voltage and current waveforms measured in Mode 3 at 60 W (half load).

Figure 21 displays the voltage and current waveforms measured in Mode 3 at 120 W (full load). The duty cycle, input voltage, output voltage, input current, and output current of S_3 were 57%, 24 V, 59 V, 5.1 A, and 2 A, respectively (Figure 21a). The voltage stress of S_3 was 90 V, and that of S_2 was 50 V; the current waveform I_{DS3} of S_3 was obtained. Furthermore, the voltage stress levels of S_3 and S_2 were 90 and 50 V, respectively (Figure 21b); Figure 21b indicates the current waveform of the battery inductance L$_{Bat}$. Figure 21c shows the voltage and current waveforms of battery and output load operated under full load.

(V$_{GS3}$ (ch1): 20 V/div; V$_{DS3}$ (ch2): 50 V/div; V$_{DS2}$ (ch3): 50 V/div; and I$_{DS3}$ (ch4): 500 mA/div)

(**a**)

Figure 21. *Cont.*

(V$_{GS3}$ (ch1): 20 V/div; V$_{DS3}$ (ch2): 50 V/div; V$_{DS2}$ (ch3): 50 V/div; and I$_{LBat}$ (ch4): 10 A/div)
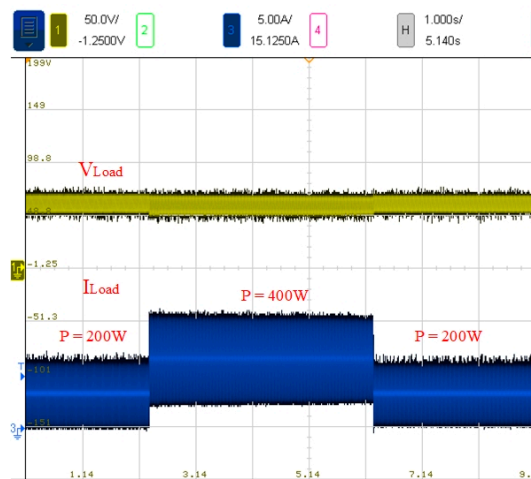
(**b**)

(V$_{Bat}$ (ch1): 20 V/div; I$_{Bat}$ (ch2): 10 A/div; V$_{Load}$ (ch3): 50 V/div; and I$_{Load}$ (ch4): 10 A/div)

(**c**)

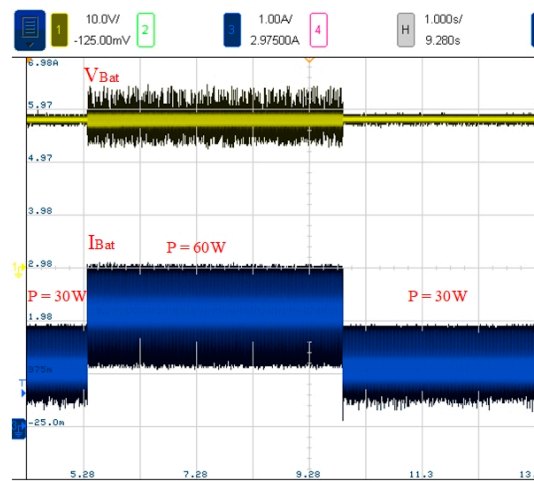**Figure 21.** Voltage and current waveforms measured in Mode 3 at 120 W (full load).

In addition, in order to verify the characteristics of the dynamic response of the proposed converter, Figure 22a,c respectively shows the measurement waveforms of the three operating modes under load variation from half load to full load, and then full load to half load.
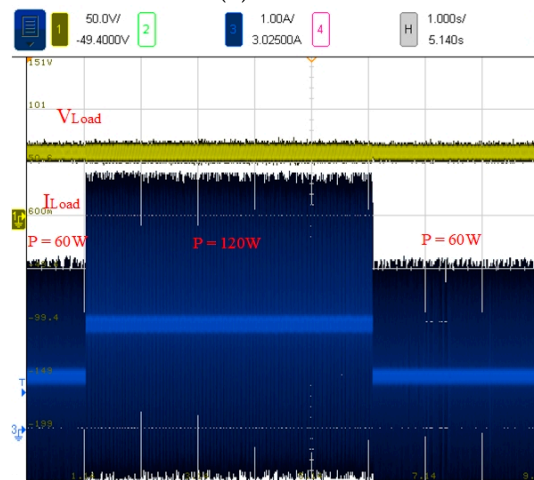

(V$_{Load}$ (ch1): 50 V/div; and I$_{Load}$ (ch3): 5 A/div)

(**a**) Mode 1

Figure 22. *Cont.*

(V_Bat (ch1): 10 V/div; and I_Bat (ch3): 1 A/div)

(**b**) Mode 2

(V_Load (ch1): 50 V/div; and I_Load (ch3): 1 A/div)

(**c**) Mode 3

Figure 22. Measured waveforms of the three operating modes under load changes, (**a**) Mode 1, (**b**) Mode 2, and (**c**) Mode 3.

It can be seen from these figures that the proposed DC/DC converter has excellent dynamic response. The load voltage (V_{load}) and battery voltage (V_{bat}) are minimally affected by load variation. Figure 23 illustrates the physical circuit of the proposed three-terminal bidirectional converter.
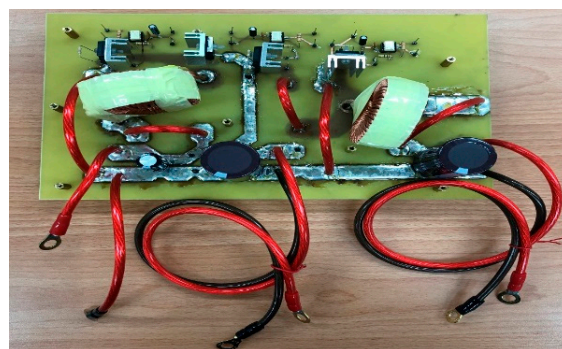

Figure 23. Proposed three-port bidirectional dc/dc converter.

To demonstrate that the proposed converter exhibits higher feasibility, higher efficiency, and a lower component count than do existing converters, this study selected converters proposed in the literature for comparison. Table 2 presents the comparison of the proposed converter with bidirectional converters in the literature. All converters involve nonisolated topologies. The number of components, input and output voltages, output power, efficiency, and number of operating modes are also presented in this table.

Table 2. Comparison of the Proposed Converter with Bidirectional Converters in the Literature.

References	Proposed Converter	Reference [25]	Reference [26]	Reference [27]
Topology	Non-Isolated	Non-Isolated	Non-Isolated	Non-Isolated
Input Voltage	24 V	24–30 V	48 V	24 V
Output Voltage	58 V	200 V	120 V	200 V
Output Power	120 W	200 W	100 W	200 W
Number of Switches	3	3	2	4
Number of Diodes	1	0	0	0
Number of Inductors	2	2	1	2
Number of Capacitors	3	1	2	3
Number of Coupled-inductors	0	1	1	1
Output Terminal	2	2	2	2
Maximum Conversion Efficiency (Step up/Step down)	96.6%/92%	91.5%/91%	95.6%/95.3%	96%/95%
Cost	Low	High	Medium	High
Converter Operational Mode	2	2	2	2

Figure 24 illustrates an efficiency comparison between the proposed converter and those in [25–27] under step-up operation. The proposed converter is shown to exhibit the highest efficiency.
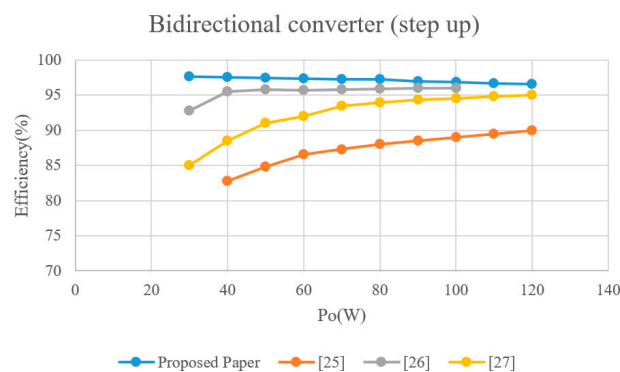

Figure 24. Efficiency comparison between the proposed converter and those in [25–27] under step-up operation.

Figure 25 displays an efficiency comparison between the proposed converter and those in [25–27] under step-down operation. The efficiency of the proposed converter is shown to be considerably higher than that of the converters in [25] and [27] but lower than that of the converter in [26].
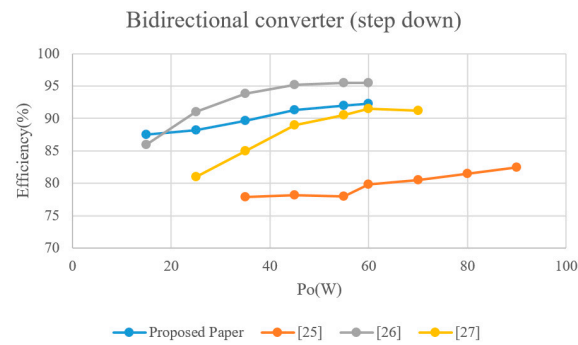
Figure 25. Efficiency comparison between the proposed converter and those in [25–27] under step-down operation.

Table 3 presents a comparison of the proposed converter with those in [28–30]. The proposed converter is shown to exhibit the highest efficiency and lowest component count. Figure 26 illustrates an efficiency comparison between the proposed converter and those in [28–30] under step-up operation. The figure indicates that the efficiency of the proposed converter is higher than that of the converters in [28–30].

Table 3. Comparison of the Proposed Converter with Other Three-Port Converters.

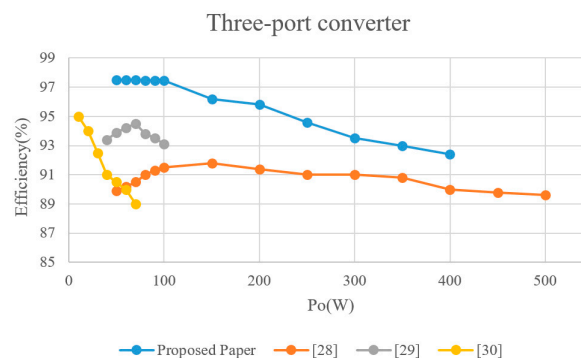| References	Proposed Converter	Reference [28]	Reference [29]	Reference [30]
Topology	Non-Isolated	Non-Isolated	Isolated	Isolated
Input Voltage	24 V	17 V	16 V	36 V
Battery Voltage	28 V	36 V	7.5 V	16 V
Load Bus Voltage	58 V	24 V	50 V	45 V
Output Power	400 W	500 W	120 W	150 W
Number of Switch	3	4	3	2
Number of Diode	1	5	4	4
Number of Transformer	0	0	1	1
Number of Inductor	2	1	2	0
Number of Capacitor	3	3	5	4
Transformer Turns	0	0	5:14	9:25
Output Terminal	2	2	2	2
Maximum Conversion Efficiency (Step-up)	96.6%	85%	94.5%	87.4%
Converter Mode	3	7	3	3

Figure 26. Efficiency comparison between the proposed converter and those in [28–30] under step-up operation.

On the basis of the preceding comparisons, the proposed converter exhibits higher efficiency and feasibility as well as a lower number of components and cost than do converters in the literature.

6. Conclusions

This paper presents a three-port bidirectional dc/dc converter for PV ES charging stations and provides a theoretical analysis of the converter under steady-state operation. Results obtained from experimental tests of the converter are also presented. The converter operates in PV step-up, battery step-up, and ES load bus step-down modes, reflecting the high functionality of the circuit. The proposed converter offers the advantages of high efficiency, three simple operating modes, small system size, low switch voltage stress and low cost. It can indeed achieve practical applications. Finally, a 400-W/60-W/120-W three-port bidirectional converter was implemented to verify its feasibility and practicability. The highest efficiency levels of the proposed converter under PV step-up, battery step-up, and step-down operation were 97.5%, 97.7%, and 92%, respectively.

References

1. Taiwan's Response to the Climate Change Framework Convention Information Network. Available online: http://www.tri.org.tw/unfccc/ (accessed on 10 September 2019).
2. Ministry of Economic Affairs. Available online: https://www.re.org.tw/default.aspx (accessed on 12 September 2019).
3. Boujelben, N.; Masmoudi, F.; Djemel, M.; Derbel, N. Design and comparison of quadratic boost and double cascade boost converters with boost converter. In Proceedings of the 2017 14th International Multi-Conference on Systems, Signals & Devices (SSD), Marrakech, Morocco, 28–31 March 2017; pp. 245–252.
4. Ismail, E.H.; Al-Saffar, M.A.; Sabzali, A.J. High Conversion Ratio DC–DC Converters with Reduced Switch Stress. *IEEE Trans. Circuits Syst. I Regul. Studys* **2008**, *55*, 2139–2151. [CrossRef]
5. Pressman, A.I.; Billings, K.; Morey, T. *Switching Power Supply Design*, 3rd ed.; Quanhua Book Company: Taipei, Taiwan, 2012.
6. Zhao, Q.; Lee, F.C. High performance coupled-inductor DC-DC converters. In Proceedings of the Eighteenth Annual IEEE Applied Power Electronics Conference and Exposition, 2003. APEC '03, Miami Beach, FL, USA, 9–13 February 2003; pp. 109–113.
7. Huber, L.; Jovanovic, M.M. A design approach for server power supplies for networking applications. In Proceedings of the APEC 2000 Fifteenth Annual IEEE Applied Power Electronics Conference and Exposition (Cat. No.00CH37058), New Orleans, LA, USA, 6–10 February 2000; pp. 1163–1169.
8. Feng, X.; Liu, J.; Lee, F.C. Impedance specifications for stable DC distributed power systems. *IEEE Trans. Power Electron.* **2002**, *17*, 157–162. [CrossRef]
9. Wu, T.F.; Yu, T.-H. Unified approach to developing single-stage power converters. *IEEE Trans. Aerosp. Electron. Syst.* **1998**, *34*, 211–223.
10. Luo, F.L.; Ye, H. Positive output super-lift converters. *IEEE Trans. Power Electron.* **2003**, *18*, 105–113.
11. Zhao, Q.; Tao, F.; Lee, F.C. A front-end DC/DC converter for network server applications. In Proceedings of the 2001 IEEE 32nd Annual Power Electronics Specialists Conference (IEEE Cat. No.01CH37230), Vancouver, BC, Canada, 17–21 June 2001; pp. 1535–1539.
12. Chen, F.; Amirahmadi, A.; Batarseh, I. Zero voltage switching Forward-Flyback Converter with efficient active LC snubber circuit. In Proceedings of the 2014 IEEE Applied Power Electronics Conference and Exposition—APEC 2014, Fort Worth, TX, USA, 16–20 March 2014; pp. 2041–2047.
13. EPARC. *Power Electronics Review*, 2nd ed.; Quanhua Book Company: Taipei, Taiwan, 2013.
14. Hart, D.W. *Power Electronics*; Quanhua Book Company: Taipei, Taiwan, 2013.

15. Jianhua, W.; Fanghua, Z.; Chunying, G.; Ran, C. Modeling and analysis of a buck/boost bidirectional converter with developed PWM switch model. In Proceedings of the 8th International Conference on Power Electronics—ECCE Asia, Jeju, Korea, 30 May–3 June 2011; pp. 705–711.

16. Mohammadi, M.R.; Farzanehfard, H. A new bidirectional ZVS-PWM Cuk converter with active clamp. In Proceedings of the 2011 19th Iranian Conference on Electrical Engineering, Tehran, Iran, 17–19 May 2011; pp. 1–6.

17. Dimna Denny, C.; Shahin, M. Analysis of bidirectional SEPIC/Zeta converter with coupled inductor. In Proceedings of the 2015 International Conference on Technological Advancements in Power and Energy (TAP Energy), Kollam, India, 24–26 June 2015; pp. 103–108.

18. Song, Y.; Enjeti, P.N. A new soft switching technique for bi-directional power flow, full-bridge DC-DC converter. In Proceedings of the Conference Record of the 2002 IEEE Industry Applications Conference. 37th IAS Annual Meeting (Cat. No.02CH37344), Pittsburgh, PA, USA, 13–18 October 2002; pp. 2314–2319.

19. Ma, Z.; Hu, R. Zero-voltage-switching condition of isolated-type symmetrical half-bridge bidirectional DC/DC converter. In Proceedings of the 2011 International Conference on Electrical and Control Engineering, Yichang, China, 16–18 September 2011; pp. 2347–2350.

20. Duan, R.; Lee, J. High-efficiency bidirectional DC-DC converter with coupled inductor. *IET Power Electron.* **2012**, *5*, 115–123. [CrossRef]

21. Wai, R.; Liaw, J. High-Efficiency-Isolated Single-Input Multiple-Output Bidirectional Converter. *IEEE Trans. Power Electron.* **2015**, *30*, 4914–4930. [CrossRef]

22. Zhang, B.; Wang, P.; Bei, T.; Li, X.; Che, Y.; Wang, G. Novel topology and control of a non-isolated three port DC-DC converter for PV-battery power system. In Proceedings of the 2017 20th International Conference on Electrical Machines and Systems (ICEMS), Sydney, Australia, 11–14 August 2017; pp. 1–6.

23. Li, W.; Xu, C.; Luo, H.; Hu, Y.; He, X.; Xia, C. Decoupling-Controlled Triport Composited DC/DC Converter for Multiple Energy Interface. *IEEE Trans. Ind. Electron.* **2015**, *62*, 4504–4513. [CrossRef]

24. Hu, Y.; Xiao, W.; Cao, W.; Ji, B.; Morrow, D.J. Three-Port DC–DC Converter for Stand-Alone Photovoltaic Systems. *IEEE Trans. Power Electron.* **2015**, *30*, 3068–3076. [CrossRef]

25. Das, P.; Mousavi, S.A.; Moschopoulos, G. Analysis and Design of a Nonisolated Bidirectional ZVS-PWM DC–DC Converter with Coupled Inductors. *IEEE Trans. Power Electron.* **2010**, *25*, 2630–2641. [CrossRef]

26. Do, H. Nonisolated Bidirectional Zero-Voltage-Switching DC–DC Converter. *IEEE Trans. Power Electron.* **2011**, *26*, 2563–2569. [CrossRef]

27. Liang, T.; Lee, J. Novel High-Conversion-Ratio High-Efficiency Isolated Bidirectional DC–DC Converte. *IEEE Trans. Ind. Electron.* **2015**, *62*, 4492–4503. [CrossRef]

28. Cheng, T.; Lu, D.D.; Qin, L. Non-Isolated Single-Inductor DC/DC Converter with Fully Reconfigurable Structure for Renewable Energy Applications. *IEEE Trans. Circuits Syst. Ii Express Briefs* **2018**, *65*, 351–355. [CrossRef]

29. Zeng, J.; Qiao, W.; Qu, L. An Isolated Three-Port Bidirectional DC–DC Converter for Photovoltaic Systems with Energy Storage. *IEEE Trans. Ind. Appl.* **2015**, *51*, 3493–3503. [CrossRef]

30. Uno, M.; Oyama, R.; Sugiyama, K. Partially Isolated Single-Magnetic Multiport Converter Based on Integration of Series-Resonant Converter and Bidirectional PWM Converter. *IEEE Trans. Power Electron.* **2018**, *33*, 9575–9587. [CrossRef]

31. Wu, Y.-E.; Chiu, P.-N. A High-Efficiency Isolated-Type Three-Port Bidirectional DC/DC Converter for Photovoltaic Systems. *Energies* **2017**, *10*, 434. [CrossRef]